Title
Analysis and Multi-Dimensional Modeling of Lithium-Air Batteries

Journal
Journal of The Electrochemical Society, 162(1)

ISSN
0013-4651

Authors
Wang, Yun
Cho, Sung Chan

Publication Date
2015

DOI
10.1149/2.0731501jes

Peer reviewed

Journal of The Electrochemical Society, **162** (1) A114-A124 (2015)
0013-4651/2015/162(1)/A114/11/$31.00 © The Electrochemical Society

Analysis and Multi-Dimensional Modeling of Lithium-Air Batteries

Yun Wang*,z and Sung Chan Cho

Renewable Energy Resources Lab (RERL), Department of Mechanical and Aerospace Engineering, The University of California, Irvine, California 92697-3975, USA

This study contributes to: 1) a multi-dimensional model framework of lithium-air (Li-air) battery, 2) incorporation of mechanisms of insoluble precipitates' impacts, and 3) analysis and discussion on oxygen supply channel for Li-air battery. The model consists of a set of partial differential equations of species and charge conservation, in conjunction with the electrochemical reaction kinetics, and takes into account the two major mechanisms of voltage loss caused by insoluble discharge products: namely, electrode passivation and increased oxygen transport resistance. Two-dimensional (2-D) simulation indicates that the pore space in the cathode electrode is not fully utilized for Li compounds storage, particularly under high discharging current. For selected battery designs, considerable variation of quantities is observed only in the thickness direction. Through analysis, we evaluate the oxygen concentration drop along an oxygen supply channel and relate it to the Damköhler (Da) number, and further explore potential cases that yield oxygen starvation.

Manuscript submitted July 30, 2014; revised manuscript received October 6, 2014. Published November 20, 2014.

Lithium-based batteries have received a great deal of research attention in recent years owing to their relatively high efficiency and energy density. A major hurdle to their development, however, is the insufficient low energy capability as opposed to fossil fuels. The gasoline's specific energy is about 13,000 Wh/kg, an order-of-magnitude higher than that of Li-ion batteries. Li-air batteries are an emerging area with a great promise of high specific energy storage. Their theoretical specific energy reaches around 11,680 Wh/kg, comparable to gasoline and higher than methanol. Their unique feature is that the cathode active material–oxygen is obtained from the ambient environment, and the anode uses lithium metal, rather than Li intercalated graphite (LiC6) as that in Li-ion batteries. Figure 1 shows schematic of a Li-air battery and its discharging operation.

Electrolyte materials and air electrodes are a central issue in Li-air battery development. Both aqueous and non-aqueous electrolytes have been studied for Li-air batteries. The type of electrolyte determines the detail of electro-chemical reactions. Below gives an example for aqueous and non-aqueous electrolyte, respectively:

$$\text{Aqueous}: \quad 2Li + \frac{1}{2}O_2 + H_2O \leftrightarrow 2LiOH \qquad [1]$$

$$\text{Non}-\text{aqueous}: \quad 2Li + O_2 \leftrightarrow Li_2O_2 \qquad [2]$$

In aqueous electrolytes, Li oxides are generally soluble. A challenge is to develop good Li^+ conducting membranes that prevent water from transporting to the anode and consequently vigorously reacting with lithium metal. Visco et al.[1] proposed NASICON (Na^+ superionic conductor)-type lithium-conducting solid glass ceramic for water-stable lithium electrodes; and Ohara Inc. used LTAP ($Li_{1+x+y}Ti_{2-x}Al_xP_{3-y}Si_yO_{12}$) glass ceramic.[2,3] Using non-aqueous electrolyte relaxes the membrane requirement for lithium metal protection. A typical example is organic carbonates, such as ethylene carbonate (EC) and propylene carbonate (PC).[4] However, the discharging products of lithium oxides/compounds are usually low in solubility in non-aqueous electrolytes, and thus precipitate at reaction sites, reducing battery efficiency and capability.

Electrolyte properties play a critical role in battery performance. The ionic conductivity of common electrolytes is around $10^{-4}\sim 10^{-3}$ S/cm, see Table I. Electrolyte decomposition and oxidation of Li compounds may not be reversible for some electrolyte (e.g. alkyl carbonates) because the pathways of reduction (discharge) and oxidation (charge) differ.[5] Solvent combination of various materials such as ethylene carbonate, ethers, and glymes has also been investigated for better electrolyte properties.[6,7] Zhang et al. blended a non-hydrolytic salt $LiSO_3CF_3$ in the PC/tris (2,2,2-trifluoroethyl) phosphate (TFP) solvent as electrolyte.[8] They evaluated viscosity, the ionic conductivity, and the discharge performance to explore optimal electrolyte composition.

Air cathodes are a major area of study in non-aqueous Li-air battery. In cathodes, Li compounds such as Li_2O_2 or Li_2CO_3 are produced during discharging. These substances in general have low solubility in major non-aqueous electrolytes, therefore precipitate at the reaction surface. They are also poor electric conductor, causing electrode passivation.[9] As discharging proceeds, the precipitates accumulate inside the pore network, deteriorating voltage drop. Several experimental works were attempted to explore electrode structure and insoluble discharge products. Albertus et al.[9] measured the battery performance for both flat (glassy carbon) and porous cathodes. Their results indicated that discharge products are electronically resistive, limiting their thickness to tens of nanometers and their volume fraction in one of their porous electrodes to a few percent. They concluded that electrical passivation is the dominant capacity-limiting mechanism in their cells. Mirzaeian and Hall[10] used porous activated carbons as cathode active materials, which were synthesized through polycondensation of resorcinol with formaldehyde followed by carbonization and activation. They investigated the effect of carbon morphology, including pore volume, pore size and surface area, on battery performance, and found that a large pore volume and wide pore size might yield better performance. Tran et al.[11] indicated a nearly linear relationship between the capacity and average pore diameter for non-aqueous electrolyte. They also pointed out that lithium oxides tend to block small pores, preventing them from further utilization in the electrochemical reaction; and would accumulate inside large pores until the density of oxides becomes high enough to choke-off the mass transfer. Xiao et al.[12] used hierarchically arranged porous Graphene sheets as air electrode, indicating that the defects and functional groups on graphene favor the formation of isolated nanosized Li_2O_2 particles and hence help prevent air blocking in cathode. Cheng and Scott[13] reported prolonged cycle life (over 200 cycles) with large capability using a nanoporous three-dimensional gas diffusion electrode. Viswanathan et al. studied the electric conductivity of Li_2O_2,[14] and used the Fc/Fc+ redox couple[15] to probe electric resistance of precipitate films. They showed "sudden death" during discharge operation occurs when the film thickness is ~5 to 10 nm. Lu et al.[16] studied Au-catalyzed Vulcan carbon electrodes, using X-Ray diffraction (XRD) and absorption. They has been suggested that the observed reduction in discharge voltage and capacity when increasing current is attributed to the resistance associated with solid-state Li^+ diffusion in the Li peroxide. Nanda et al.[17] investigated the three-dimensional spatial distribution of lithium products using neutron tomographic imaging. More lithium products were observed near the electrode's edge. Gallant et al.[18] examined chemical and morphological change of reaction products during cycling using X-ray absorption, selected area electron diffraction (SAED), and transmission electron microscopy (TEM).

*Electrochemical Society Active Member.
zE-mail: yunw@uci.edu

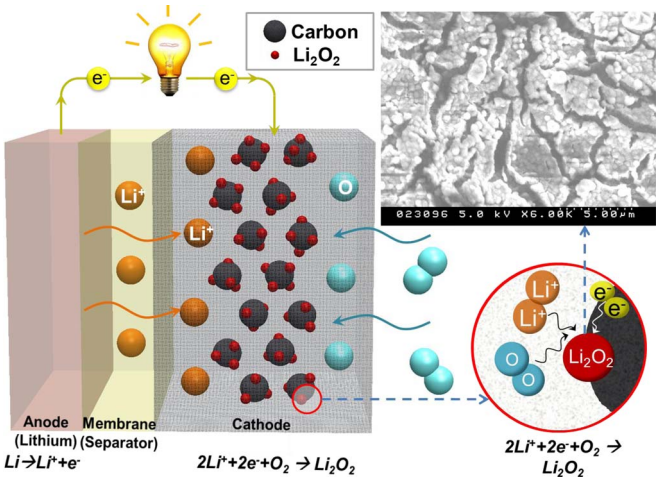

Figure 1. Schematic of a Li-air battery and its discharging operation with Li_2O_2 as an example of discharge product. The SEM image in the upper right was taken for precipitate over highly ordered pyrolytic graphite (HOPG) at 10 $\mu A/cm^2$ for 1M LiTriflate in DOL:DME (1:1 w/w).

In the modeling aspect, Albertus et al. proposed a 1-D model study.[9] Their model was built upon the modeling framework of Li-ion batteries and took into account the passivation effect due to insoluble discharge product formation over spherical particles. A good match was achieved between porous-electrode experiment and simulation by using an empirical fit to the resistance of the discharge products obtained from flat-electrode experiment. Andrei et al.[19] presented a 1-D model and simulated a Li-air battery consisting of organic electrolyte at the anode and aqueous electrolyte at the cathode. They investigated two scenarios to study the dependency of specific capacity and power densities on the geometrical and material parameters. Ren et al.[20] examined cathode performance for different carbon materials. An ORR mechanistic model that accounts for reaction products deactivating the catalytic sites was proposed. Sahapatsombut et al.[21] proposed a model to predict electrolyte degradation and cycling behaviors, which assumed that Li_2O_2 and Li_2CO_3 are the final discharge products. Wang[22] stressed out that the physics of lithium oxides precipitation is similar to water freezing in PEM fuel cells under sub-freezing condition; and proposed several modes of precipitation growth. They further formulated the voltage loss due to precipitates and presented a surface coverage approach to model insoluble product formation. Wang and Cho[23] further took into account oxygen diffusion in the cathode, and analyzed the voltage loss mechanisms due to oxygen starvation and surface coverage. The analytical results agreed well with several literature data.

Despite the great efforts in Li-air battery development and modeling, few works have been reported on multi-dimensional modeling and associated analysis. Previous 1-D or lumped models consider relatively ideal conditions, and thus limit their prediction capability. Multi-dimensional approach is necessary to simulate practical Li-air battery operation. For example, in high specific power applications (power per volume) or battery pack, oxygen distribution is likely non-uniform at the cathode's outer surface. In this paper, we developed one of the first multi-dimensional modeling frameworks for Li-air batteries and predicted the distributions of oxygen and reaction rates, along with battery performance. In a few designs and conditions,

Table I. Ionic conductivity of various electrolytes.[23]

Electrolyte	Ionic conductivity	Remarks
PVA (Poly Vinyl Alcohol)	$10^{-8} \sim 10^{-4}$ S/cm	PVA complexed with lithium triflate system
PC / γ-BL (propylenecarbonate / γ-butyrolactone)	1.7×10^{-3} S/cm	60P(ECH-EO):15PC:10γ-BL:15$LiClO_4$ @ 363K
DMF / γ-BL dimethylformamide / γ-butyrolactone)	2.8×10^{-3} S/cm	60P(ECH-EO):15DMF:10γ-BL:15$LiClO_4$ @ 363K
PVA(15)–PMMA(10)–LiBF4(8)– EC(67)	9.0377×10^{-3} S/cm	@373K
PVA(15)–PMMA(10)–LiBF4(8)– PC(67)	2.4855×10^{-3} S/cm	
PVA(15)–PMMA(10)–LiBF4(8)– DEC(67)	0.2022×10^{-3} S/cm	
PVA(15)–PMMA(10)–LiBF4(8)– GBL(67)	1.1523×10^{-3} S/cm	
PVdF-HFP	2×10^{-3} S/cm	
PVC / PMMA	1.4×10^{-3} S/cm	@ room temperature
PAN(21)–PEO(2)– $LiCF_3SO_3$ (8)–PC(27.7)–EC(41.3)	1.713×10^{-3} S/cm	@373 K
PAN(21)–PEO(5)– $LiCF_3SO_3$ (8)–PC(24.7)–EC(41.3)	8.492×10^{-3} S/cm	
PAN(21)–PEO(10)– $LiCF_3SO_3$ (8)–PC(27.7)–EC(33.3)	80.950×10^{-3} S/cm	
PAN(21)–PEO(15)– $LiCF_3SO_3$ (8)–PC(24.7)–EC(31.3)	23.880×10^{-3} S/cm	
EC(38) –PC(33) –PAN(21) –$LiClO_4$(8)	3.5×10^{-3} S/cm	@323 K
EC(42) –PC(36) –PAN(15) –$LiCF_3SO_3$(7)	2.2×10^{-3} S/cm	
EC(62) –PC(13) –PAN(16) –PEGDA(1) –$LiClO_4$(8)	3.0×10^{-3} S/cm	
EC(68) –PC(15) –PEGDA(3) –$LiClO_4$(14)	8.0×10^{-3} S/cm	
EC(35) –PC(31) –PVP(24)–$LiCF_3SO_3$ (10)	1.0×10^{-3} S/cm	
EC–$LiClO_4$	$10^{-8} \sim 10^{-7}$S/cm	[EC]/[$LiClO_4$] = 0.5 @ 298 K
	10^{-6}S/cm	[EC]/[$LiClO_4$] = 1.0 @ 298 K
	$10^{-5} \sim 10^{-4}$ S/cm	[EC]/[$LiClO_4$] = 2.0 @ 298 K
PEO(22.7) –PAN(17.4) –PrC(7.3) –EC(8.5) –$LiClO_4$(4.3)	0.37×10^{-3} S/cm	HSPE @ 303 K
PEO(22.7) –PrC(13.3) –$LiClO_4$(1.2)	0.84×10^{-3} S/cm	PEO + PrC @ 303 K
PAN(23.2) –PrC(24.5) –EC(28.4) –$LiClO_4$(3.0)	1.34×10^{-3} S/cm	PAN + PrC + EC @ 303 K
PC-DME	10^{-3} S/cm	(1:1 by wt.) plasticized P($LiOEG_nB$) n = 3, 5, 9
	12×10^{-3} S/cm	(1:1 by vol.) 1M $LiClO_4$ @ 293 K
	14×10^{-3} S/cm	(1:1 by vol.) 1M $LiPF_6$ @ 293 K
EC-DMC	8×10^{-3} S/cm	(1:1 by vol.) 1M $LiClO_4$ @ 293 K
	10×10^{-3} S/cm	(1:1 by vol.) 1M $LiPF_6$ @ 293 K
	11.7×10^{-3} S/cm	(1:1 by mol) 1M $LiPF_6$ @ 303 K
	$< 10^{-3}$ S/cm	(1:2 by wt.) plasticized P($LiOEG_nB$) n = 3
DME	5.52×10^{-3} S/cm	1mol LiF + 1mol $(C_6F_5)_3B$ in DME
	7.43×10^{-3} S/cm	1mol CF_3CO_2Li + 1mol $(C_6F_5)_3B$ in DME
	5.52×10^{-3} S/cm	1mol $C_2F_5CO_2Li$ + 1mol $(C_6F_5)_3B$ in DME

considerable variation was only observed in the thickness direction, which verifies the previous 1-D approach. We also identified and present a few of cases that show considerable oxygen variation over the cathode outer surface through both analysis and simulation.

Mathematical Model

Figure 1 presents the schematic of Li-air battery discharging, and the constituent components to be modeled in this work. The model consists of a set of conservation equations of species oxygen, Li^+, and electrons, in conjunction with the electrochemical reaction kinetics. The following assumptions are made: 1) side reactions are ignored; 2) porous electrodes are isotropic and homogeneous; 3) equilibrium between electrolyte and gas phases holds true; 4) operation is isothermal; 5) the charge transfer kinetics is approximated by the Butler-Volmer equation; and 6) convective transport is negligible.

Electrochemical kinetics.— The cathode electrode consists of multiple materials, including electrolyte, carbon, and support materials (e.g. Ni mesh). The oxygen reduction reaction (ORR) is the major reaction, taking place at the interface between the electrolyte and electrode. An example is:

$$2Li^+ + O_2 + 2e^- \rightarrow Li_2O_2 \qquad (E_{rev} = 2.96\,V \text{ vs Li}) \qquad [3]$$

The potential value E_{rev} was derived from published Gibbs free energy database.[24–26] In major non-aqueous electrolytes, Li_2O_2 is extremely low in solubility, and thus precipitates at local reaction site. Note that the ORR is complex, usually involving multiple steps. For the ORR in dimethyl sulfoxide (DMSO)/$LiPF_6$ Electrolytes, the following steps were suggested[27]:

$$\begin{aligned} &\text{step 1}: \quad O_2 + Li^+ + e^- = LiO_2 \\ &\text{step 2}: \quad 2LiO_2 = Li_2O_2 + O_2 \text{ (chemical)} \\ &\text{step 3}: \quad LiO_2 + Li^+ + e^- = Li_2O_2 \\ &\text{step 4}: \quad Li_2O_2 + 2\,Li^+ + 2e^- = 2Li_2O \end{aligned} \qquad [4]$$

In a few electrolytes, Li_2CO_3 or LiOH is the major final product, and both substances have low solubility in non-aqueous electrolytes.

In the anode, Li ions and electrons are produced:

$$Li \rightarrow Li^+ + e^- \qquad [5]$$

Assuming a one-step reaction, the electrochemical rate is approximated by the Butler-Volmer equation. For an *n*-electron process, it is given by:

$$\begin{aligned} j &= ai_0 \left\{ \exp\left(\frac{1-\beta}{RT} \cdot F \cdot \eta\right) - \exp\left(-\frac{\beta}{RT} \cdot F \cdot \eta\right) \right\} \\ &= anFk \left\{ \exp\left(\frac{1-\beta}{RT} \cdot F \cdot \eta\right) - \exp\left(-\frac{\beta}{RT} \cdot F \cdot \eta\right) \right\} \end{aligned} \qquad [6]$$

where β is the charge transfer coefficient. The right side on the above equation was adopted by Albertus et al.: for the anode, n = 1; while n = 3 for the cathode.[9] Later, we will give a specific expression for the cathode ORR kinetics. The exchange current density i_0 is determined by the electrochemical kinetics, while the surface-to-volume ratio *a* measures the roughness of porous electrodes.

In the cathode, insoluble products are deposited at the reaction surface, leading to electrode passivation. In our previous work,[22] we derived that the electrode passivation is equivalent to loss in reaction surface area:

$$a = (1-s)^{\tau_a} a_0 \qquad [7]$$

in which *s* is defined as the volume fraction of insoluble products in the void space. For the spherical-shell growth mode of precipitates, the exponent coefficient τ_a, a surface coverage factor, is given by[22]:

$$\tau_a = -\frac{I(1-\beta)F}{a_0 RT \ln\left(1-\frac{\varepsilon_{prod}}{\varepsilon}\right)} \left\{ A_0 \left[\sqrt[1/3]{1+\frac{\varepsilon_{prod}}{\varepsilon_{carbon}}} - 1 \right] r_{carbon} + R_0 \right\} \qquad [8]$$

where R_0 is the contact resistance between the carbon particle and deposit shell. It is seen that τ_a is proportional to current density *I* and is a function of the volume fraction of insoluble product ε_{prod}. Because a porous electrode intrinsically contains various morphology of reaction interfaces, the following form of τ_a was proposed[22] and adopted in the present paper to account for the effects of current density and insoluble product volume fraction:

$$\tau_a = \begin{cases} B_1 \dfrac{I}{I_0} & s < s_0 \quad \text{where s} = \dfrac{\varepsilon_{prod}}{\varepsilon} \\ \dfrac{I}{I_0}\left[B_1 + B_2(s-s_0)\right] & \text{otherwise} \end{cases} \qquad [9]$$

Physically, B_1 represents the effect of the reaction surface area a_0, transfer coefficient β, and other factors on the coverage factor. A larger area of a_0 will yield smaller surface coverage (or smaller B_1). B_2 is determined by the effect of precipitate film formation, which imposes a larger impact than the initial heterogeneous nucleation. s_0 is the precipitate's volume fraction in which transition from heterogeneous nucleation to film formation occurs. I_0 is a reference current, introduced to render B_1 dimensionless.

In Li-air batteries, the ORR is sluggish, yielding a large cathode overpotential. The Butler-Volmer equation can be approximated by Tafel kinetics:

$$\begin{aligned} j_c &= -ai_{0,c}^{ref} C_{O2}^{1-\beta} C_e^{1-\beta} \exp\left(-\frac{1-\beta}{RT} F\eta\right) \\ &= -anFk{C_{O2}}^{1-\beta}{C_e}^{1-\beta} \exp\left(-\frac{1-\beta}{RT} F\eta\right) \end{aligned} \qquad [10]$$

where the surface overpotential is defined as:

$$\eta = \Phi^{(s)} - \Phi^{(e)} - E_o \qquad [11]$$

E_o (V) is the equilibrium potential. In some works, electrode passivation due to precipitates was modeled through adding a ohmic voltage loss[9]:

$$\eta = \Phi^{(s)} - \Phi^{(e)} - E_o - i_n R_{prod} \qquad [12]$$

where i_n is the current density across the discharge film at the direction normal to the reaction surface and the resistance R_{prod} is given by:

$$R_{prod} = A_0 l + R_0 \qquad [13]$$

where *l* is the precipitate film thickness, determined by the precipitates volume ε_{prod} and growth modes.[22]

In the anode, we assume the produced Li ions immediately enter the separator toward the cathode. As no discharging products precipitate, the overpotential is calculated by Eq. 11 directly.

Species conservation equations.— In Li-air battery, both oxygen and Li ions are delivered toward the reaction site. In porous cathodes, the pore-network structure provides the passage for oxygen and Li ion transport. In common operation, no external forces are imposed to promote electrolyte bulk flows, thus convection is unimportant. The separator has low oxygen diffusivity to prevent oxygen access to the anode. The conservation equation for oxygen transport in these three components is unified as:

$$\frac{\partial \varepsilon C_{O2}}{\partial t} = \nabla \cdot \left(D_{O2}^{eff} \nabla C_{O2}\right) + S_{O2} \qquad [14]$$

where the effective diffusion coefficient D_{O2}^{eff} is evaluated through[28,29]:

$$D_{O2}^{eff} = \varepsilon^{\tau} D_{O2} \quad \text{or} \quad D_{O2}^{eff} = \frac{\varepsilon}{\tau'} D_{O2} \qquad [15]$$

The former is the well-known Bruggeman relation; the latter clearly shows the physics of tortuosity, see Figure 2. In this study, we follow the Bruggeman relation. In the cathode, oxygen dissolves in liquid electrolytes and diffuses toward reaction surface. In general, molecule diffusion in liquids can be evaluated using a hydrodynamic model that assumes the resistance of solute molecule movement arises from the

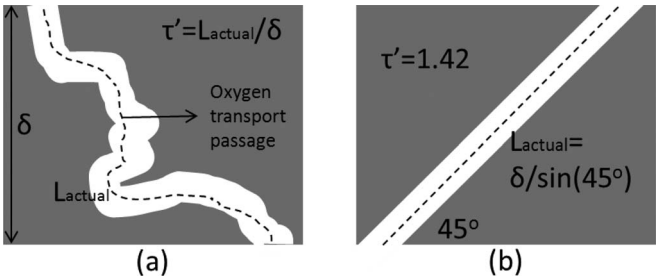

Figure 2. Illustration of oxygen transport passage and tortuosity.

Table II. Oxygen diffusivity in nonaqueous electrolytes.

Oxygen diffusivity	Electrolyte	Reference
7.0×10^{-6} cm^2/s	1M $LiPF_6$ in PC:DME (1:1)	40
4.0–4.5 $\times 10^{-5}$ cm^2/s	CCl_4	41
5.1–5.5 $\times 10^{-5}$ cm^2/s	CS_2	41
2.9–3.4 $\times 10^{-5}$ cm^2/s	$C_2H_4CL_2$	41
1.3–1.7 $\times 10^{-5}$ cm^2/s	CH_2CL_2	41
9.75×10^{-6} cm^2/s	0.1M $TBAPF_6$ in DMSO	27
2.45×10^{-5} cm^2/s	0.1M $TBAPF_6$ in MeCN	27
1.67×10^{-5} cm^2/s	0.1M $LiPF_6$ in DMSO	27
4.64×10^{-6} cm^2/s	0.1 M $LiPF_6$ in MeCN	27
1.22×10^{-5} cm^2/s	0.1M $LiPF_6$ in DME	27
3.88×10^{-6} cm^2/s	0.1M $TBAPF_6$ in DME	27
2.17×10^{-6} cm^2/s	0.1M $LiPF_6$ in TEGDME	27
4×10^{-5} cm^2/s	1M Li^+ in DME	16
9×10^{-6} cm^2/s	1M Li^+ in PC:DME(1:2)	16
2.2×10^{-6} cm^2/s	1M L:i^+ in PC	16
2.2×10^{-5} cm^2/s	0.1M $TBAClO_4$	42
2.1×10^{-5} cm^2/s	0.1M $TBAPF_6$	42
4.87×10^{-5} cm^2/s	0.9M $TEABF_4$	45
2.07×10^{-5} cm^2/s	0.1M TEAP	46

viscous force, similar to particle movement in viscous fluids. In dilute liquids, the approach yields the famous Stokes-Einstein equation:

$$D^0 = \frac{k_B T}{6\pi r \mu} \quad [16]$$

where k_B is the Boltzmann's constant, r the radius of oxygen molecule, and μ the electrolyte viscosity. In a solution that is not infinitely dilute, modification can be made by introducing the volume fraction of solute ε_i[29,30]:

$$D^{0*} = D^0(1 + 1.45\varepsilon_i) \quad [17]$$

Table II lists oxygen diffusivity in a few electrolytes, showing its value approximates 10^{-5} cm^2/s.

In Eq. 15, tortuosity τ (or τ') measures the actual length of diffusion passage in a porous medium, see Figure 2. In addition, the

Table IV. Source terms in the governing equations.

	S_{O2}	S_{Ce}	$S_{\Phi^{(e)}}$	$S_{\Phi^{(s)}}$
Gas channel	0	–	–	–
Porous electrode	$\frac{j_c}{4F}$	$-\nabla \cdot \left(\frac{\vec{i}_e(1-t_+)}{F}\right)$	j_c	$-j_c$
Separator	0	0	0	–

MacMullin number (N_M), defined as the ratio of resistance of porous media saturated with an electrolyte to the bulk resistance of the same electrolyte, also measures the effectiveness of species transport[31,32]:

$$N_M = \frac{D_k}{D_k^{eff}} = \frac{1}{f(\varepsilon, \tau)} \quad [18]$$

In Eq. 15, the MacMullin number is implicitly defined as $\varepsilon^{-\tau}$ and $\frac{\tau'}{\varepsilon}$, respectively. Table III lists the expression of N_M for various porous media as a function of ε. In general, $f(\varepsilon, \tau)$ is determined by the pore structure such as pore morphology and arrangement.

At the interface between electrolyte and air where oxygen dissolves and enters the electrolyte during discharging, Henry's law applies, which states that the amount of a gas dissolving in a liquid is proportional to the partial pressure of that gas in equilibrium with the liquid. The relationship can be written as:

$$C_{O2,e} = k_{H,cc} C_{O2,g} \quad [19]$$

where $k_{H,cc}$ is the Henry's constant.

Conservation of Li^+ species in the electrolyte phase is given by:

$$\frac{\partial \varepsilon C_e}{\partial t} = \nabla \cdot \left(D_e^{eff} \nabla C_e\right) + S_{Ce} \quad [20]$$

In the cathode, the effective diffusion coefficient D_e^{eff} is given by:

$$D_e^{eff} = \varepsilon^{\tau} D_e \quad \text{or} \quad D_e^{eff} = \frac{D_e}{N_M} \quad [21]$$

and[32]:

$$D_e = 0.00003018 \times \exp(0.357 C_e) \quad [22]$$

where D_e is in cm^2/s and C_e is in mol/liter.

The source term S_{Ce} describes the migration and reaction consumption/production rate, see Table IV, where t_+ is the transference number, defined as the fraction of the current that is carried by Li ions. Table V lists the range of t_+ in a few electrolytes. In this study, we adopted the correlation below for the transference number[33]:

$$t_+ = 0.4492 - 0.4717 C_e + 0.4106 C_e^2 - 0.1287 C_e^3 \quad [23]$$

Conservation of insoluble discharge products.— Assuming all the discharge products are insoluble, they will precipitate inside the cathode's pore network during discharging, and their volume fraction is

Table III. MacMullin number (N_M) of a system consisting of a dispersed non-conducting phase in a conductive medium.[30,31]

Label	Geometry	Arrangement	Size	Expression
I	Spheres	Random	Uniform	$N_M = \frac{(5-\varepsilon)(3+\varepsilon)}{8(1+\varepsilon)\varepsilon}$
II	Spheres	Cubic lattice	Uniform	$N_M = \frac{(3-\varepsilon)\left[\frac{4}{3} + 0.409(1-\varepsilon)^{7/3}\right] - 1.315(1-\varepsilon)^{10/3}}{2\varepsilon\left[\frac{4}{3} + 0.409(1-\varepsilon)^{7/3}\right] - 1.315(1-\varepsilon)^{10/3}}$
III	Spheres	Random and ordered	Range	$N_M = \varepsilon^{-1.5}$
IV	Cylinders	Parallel (square array)	Uniform	$N_M = \frac{2 - \varepsilon - 0.3058(1-\varepsilon)^4 - 1.334(1-\varepsilon)^8}{\varepsilon - 0.3058(1-\varepsilon)^4 - 1.334(1-\varepsilon)^8}$
V	Fibrous material (Cylinders)	Random	–	$N_M = \frac{0.9126}{\varepsilon(\varepsilon - 0.11)^{0.785}}$

Table V. Li^+ transference number in nonaqueous electrolytes.

Li^+ transference number	Electrolyte	Reference
0.13	PAN(16)/PC(23)/EC(56.5)/$LiClO_4$(4.5)	43
0.34	PAN(16)/PC(23)/EC(56.5)/$LiClO_4$(10.8)	43
0.58–0.62	PAN(9)/EC(82)/LiTFSI(9)	44
0.56–0.59	PAN(14)/EC(77)/LiTFSI(9)	44
0.32	PAN(10)/EC(78)/LiTFSI(12)	44
0.28	PAN(14)/EC(72)/LiTFSI(14)	44
0.27	PAN(10)/EC(76)/LiTFSI(14)	44
0.36	PAN(10)/EC(74)/LiTFSI(16)	44
0.62	PAN(14)/EC(68)/LiTFSI(18)	44
0.4–0.5	1M Li^+ in DME	16
0.43	1M Li^+ in PC:DME(1:2)	16
0.35	1M Li^+ in PC	16
0.02–0.16	PAN(13.5)/EC(37.5/PC(37.5)/$LiAsF_6$(11.6)	47
0.16–0.34	PAN(12.8)/EC(71.4)/$LiN(CF_3SO_2)_2$(15.8)	47
0.01–0.36	PAN(14.0)/EC(38.5)/PC(38.5)/$LiPF_6$(9.0)	47

derived through conservation law[22]:

$$\frac{d\varepsilon_{prod}}{dt} = -\frac{j_c M_{prod}}{nF\rho_{prod}\varepsilon_{film}} \quad [24]$$

where ε_{film} is defined as the film's volumetric porosity. Given that the precipitate film may have a pore structure, trapping electrolyte, see Figure 1. As discharging proceeds, the electrode actual porosity decreases. Assuming the trapped electrolyte in the precipitate film is immobile, the electrode effective porosity ε is then calculated by:

$$\varepsilon = \varepsilon_0 - \varepsilon_{prod} = \varepsilon_0(1-s) \quad \text{where} \quad s = \varepsilon_{prod}/\varepsilon_0 \quad [25]$$

Charge conservation equation.— Conservation of charge gives:

$$0 = \nabla \cdot \left(\kappa^{eff}\nabla\Phi^{(e)} + \kappa_D^{eff}\nabla \ln C_e\right) + S_{\Phi^{(e)}} \quad [26]$$

where $\Phi^{(e)}$ is the electric potential in the electrolyte phase. The diffusional conductivity κ_D^{eff} is given by:

$$\kappa_D^{eff} = \frac{2RT\kappa^{eff}}{F}(1-t_+)\left(1+\frac{d\ln f_\pm}{d\ln C_e}\right) \quad [27]$$

where $f_\pm$ is the mean molar activity coefficient of the electrolyte.

In the cathode, the ionic conductivity κ is determined by the electrolyte material such as composition. Table I lists the ionic conductivity measured for major types of electrolytes. For the electrolyte LiPF6 in a 2:1 mixture of ethylene carbonate (EC) and dimethyl carbonate (DMC), the following correlation was developed through fitting with experimental data[34]:

$$\kappa = 4.1253\times10^{-4} + 5.007\times10^{-3}C_e - 4.7212\times10^{-3}C_e^2 + 1.5094\times10^{-3}C_e^3 - 1.6018\times10^{-4}C_e^4 \quad [28]$$

where C_e is in mol/dm^3 and κ in S/cm.

In the cathode electrode, the effective conductivity κ^{eff} is given by the Bruggeman relation or MacMullin number N_M:

$$\kappa^{eff} = \varepsilon^\tau\kappa \quad \text{or} \quad \kappa^{eff} = \kappa/N_M \quad [29]$$

Conservation of charge (electrons) in the solid phase follows ohm's law:

$$0 = \nabla\cdot\left(\sigma^{eff}\nabla\Phi^{(s)}\right) + S_{\Phi^{(s)}} \quad [30]$$

In porous electrodes:

$$\sigma^{eff} = (1-\varepsilon_0)^\tau\sigma \quad [31]$$

Note that insoluble products are extremely low in electrical conductivity comparing with the cathode's solid structure, and thus their presence has negligible contribution to σ^{eff}. However, insoluble products have significant impact on charge transfer at the reaction interface, which is taken into account by Eq. 8 or 9.

Boundary conditions.— For the above set of the governing equations, their corresponding boundary conditions are described as follows:

Inlet boundary.—a constant oxygen concentration (the ambient value) is set at the gas channel inlet, while others are set with no-flux condition:

$$C_{O2} = C_{O2,0} \quad \text{and} \quad \frac{\partial}{\partial n}\begin{pmatrix} C_e \\ \Phi^{(e)} \\ \Phi^{(s)}\end{pmatrix}\Bigg|_{inlet} = 0 \quad [32]$$

Walls.—No-flux conditions are applied for all the walls except the outer surface of the current collectors, where

In the cathode:

$$-\sigma\frac{\partial}{\partial n}\Phi^{(s)}\Big|_{\substack{cathode\\wall}} = I \quad [33]$$

where I is the discharging current density applied as a control parameter.

In the anode,

$$\Phi^{(s)} = 0 \quad [34]$$

Numerical procedures.— The governing equations, along with their appropriate boundary conditions, are discretized using finite volume methods (FVM).[35] The "finite volume" refers to the small volume surrounding a node point in a computational mesh. In FVMs, a volumetric integral over a partial differential conservation equation that contains a divergence term (e.g. the convective or diffusive terms) is converted to surface integrals, based on the divergence theorem. The divergence term is then evaluated through the surface fluxes in each finite volume. Below gives a brief description of the FVM discretization.

For FVM, it is convenient to unify all the governing equations, including the transient terms, in the following form:

$$\nabla\cdot\vec{\Gamma}(\Theta) = S_\Theta \quad [35]$$

where Θ stands for any dependent variable. Integrating the above equation throughout an arbitrary volume V bounded by a closed surface S yields:

$$\oint_S \vec{\Gamma}(\Theta)\cdot d\vec{S} = \int_V S_\Theta dv \quad [36]$$

where $\vec{S}$ is the surface vector. Taking V and $\vec{S}$ to be the volume V_p and discrete faces S_j of a computational cell, respectively, yields:

$$\sum_j \int_{S_j}\vec{\Gamma}(\Theta)\cdot d\vec{S} = \int_{V_p} S_\Theta dv \quad [37]$$

The final form of the discrete FVM equation is then expressed as:

$$B_p\Theta_p^n = \sum_m B_m\Theta_m^n + B(\Theta_p^0) \quad [38]$$

The above set of algebraic equations is solved by the algebraic multi-grid (AMG) method. The solver is based on our in-house FORTRAN code developed for electrochemically reactive systems. The solver specially includes efficient numerical treatment for the two phase-potential equations, which enables both current density and cell voltage virtual control over a Li-air battery. The 2-D computational domain is shown in Figure 3, which contains 400 computational elements. Grid-dependency study was performed, showing further refining the present mesh yields similar voltage prediction (difference <2%). The battery dimension, operating parameters, and physical properties are listed in Table VI. Adaptive time step is chosen: the present time step dt is inversely proportional to the voltage change in the previous time step, with the maximum time step < 1 s. In all the simulations to be presented in the next section, the equation residuals are set to be smaller than 10^{-7} in each time step. A typical case takes approximately eight hours on a single node (AMD Opteron 2.20 GHz).

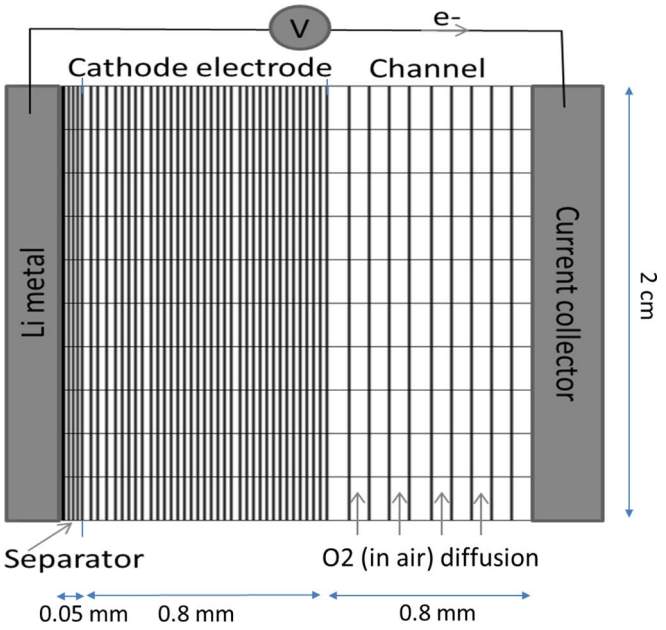

Figure 3. Computational domain of the Li-air battery.

Table VI. Physical, electrochemical, and model parameters.

Quantity	Value
Separator/electrode thickness	0.05/0.8 mm
Channel depth/length	0.8 or 0.08 mm/2 or 10 cm
Transfer coefficient β	0.5
Faraday constant	96,487 C/mol
Molecular weight of Li	6.941 g/mol
Molecular weight of O_2	32 g/mol
Tortuosity of electrode	2.0*
Temperature	298.15 K
Electrode/current collector interface resistance	100 mΩ cm^2*
Mass density of carbon	2,260 kg/m^3
Initial electrolyte concentration, C_{e0}	1,000 mol/m^3
Mass density of the electrolyte	1,114 kg/m^3
Ambient oxygen concentration, $C_{O2,0}$	8.58 mol/m^3
Open circuit potential[19]	3.4 V
Henry's constant, $k_{H,cc}$[19]	0.344
Electrical conductivity of carbon electrode	10 S/m*
Ion conductivity (κ) of separator[19]	0.1 mS/cm
Ion conductivity (κ) of electrolyte	Eq. 28
O_2 diffusivity in electrolyte[9]	1.83×10^{-9} m^2/s
O_2 diffusivity in the air $D_{O2\text{-}N2,0}$ at 273.2 K and 1 atm[37]	1.81×10^{-5} m^2/s
O_2 diffusivity in the separator[19]	10^{-9} m^2/s
Density of discharge product (Li_2O_2)	2,140 kg/m^3
Molecular weight of discharge product (Li_2O_2)	0.04588 kg/mol
Kinetic rate constant k in the positive electrode[9]	5.9×10^{-14} m/s
Kinetic rate constant k in the negative electrode[9]	6.1×10^{-6} $mol^{0.5}/m^{0.5}$ s
Transference number (t_+) in the separator[19]	1
Transference number (t_+) in the electrolyte	Eq. 23
Porosity of discharge materials ε_{film}	0.9*
Electrode initial porosity ε_0	0.75*

*Estimate for fitting the experimental data.

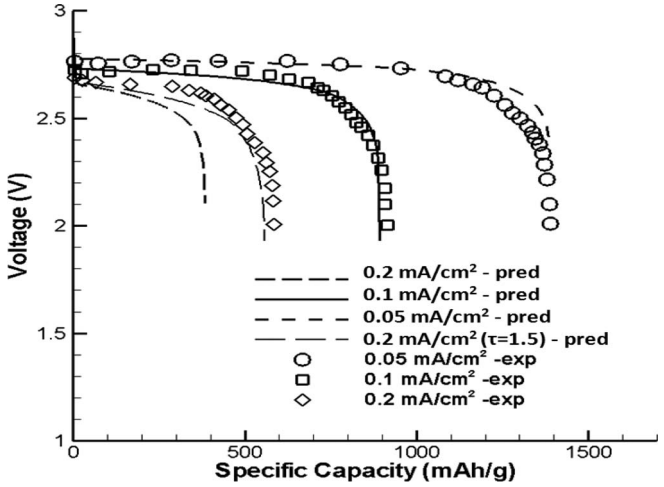

Figure 4. Comparison of the predicted discharging voltage with the experimental data in Read.[36]

Results and Discussion

For validation, we chose the experimental data from Read.[36] The model parameters and boundary conditions were set according to the experiment setup, specially the simulation considered pure oxygen and set a constant oxygen concentration at the cathode outer surface. The prediction shows acceptable agreement with experimental data, see Figure 4. In discharging, insoluble Li compounds are produced, and precipitate at local reaction site, leading to voltage loss. The voltage drop accelerates when the operation approaches the cut-off voltage (2.0 V). Our previous analysis indicated that the initial gradual decrease arises from electrode passivation, while the rapid drop in the latter stage is mainly due to the oxygen transport resistance raised by precipitate accumulation in pores.[23] Under higher current density, the voltage decreases more severely, reducing discharging capability, as expected. For 0.05 and 0.1 mA/cm^2, a same set of model parameters were used, listed in Table VI. For 0.2 mA/cm^2, using the same tortuosity (i.e. $\tau = 2.0$) fails to match with the experimental data (also plotted in the figure). Using a different tortuosity ($\tau = 1.5$) yields a prediction closer to the experimental data, see Figure 4. In reality, it is possible that the effect of insoluble precipitates varies with discharge current, yielding current-dependent tortuosity. Physically, tortuosity is a property characterizing transport passage. Precipitates partially occupy the passage space, narrowing down the passage and likely altering the passage shape. The latter is dependent on the precipitates' morphology. In Li-air battery, precipitates are produced more rapidly under higher discharge current, thus it is possible the deposit film is more firmly packed or has less surface roughness, yielding smaller impact on transport route. As direct evidence, Figure 5 displays the SEM images of precipitates over the same planar surface under two

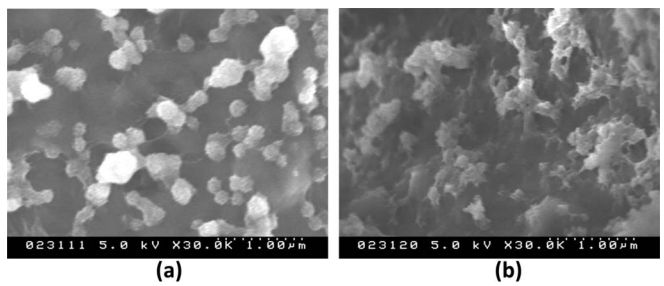

Figure 5. SEM images of the precipitate's morphology for: (a) 10 $\mu A/cm^2$ and (b) 20 $\mu A/cm^2$; over highly ordered pyrolytic graphite (HOPG) for 1M LiTriflate in DOL:DME (1:1 w/w).[39]

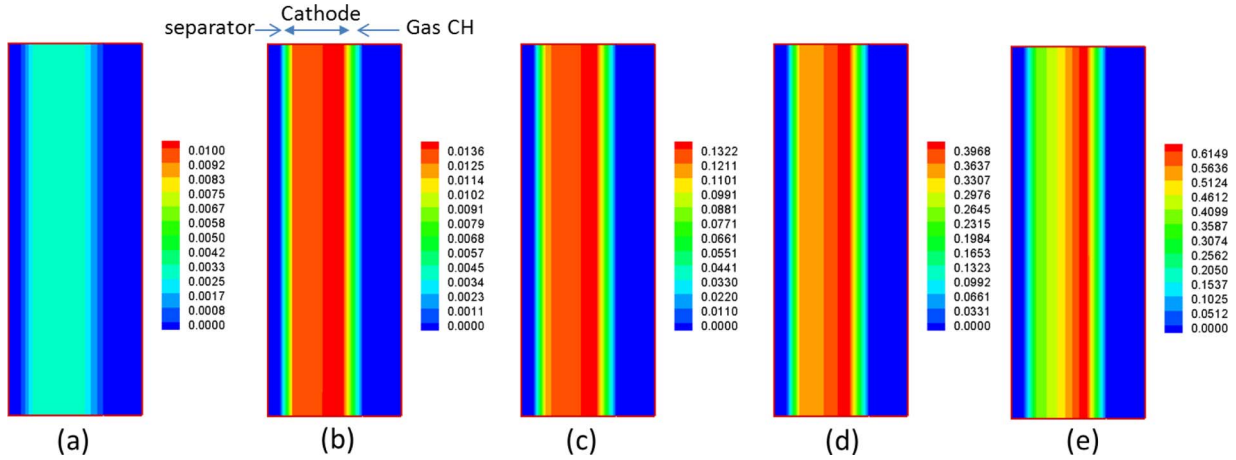

Figure 6. Precipitate volume fraction inside the cathode under the discharging current of 0.05 mA/cm^2 at the stage of (see Figure 4): (a) 7.5 mAh/g; (b) 37.5 mAh/g; (c) 360 mAh/g; (d) 1080 mAh/g; (e) 1360 mAh/g.

discharge currents, showing difference in the precipitate's morphology and hence tortuosity. In addition, other factors such as composition variation may contribute to the discrepancy observed between the model prediction and experimental result. Furthermore, it is possible that tortuosity is a function of discharging time because the buildup of precipitates may greatly alter the morphology of pore network. It is however extremely difficult to measure the time dependency. Thus, we assume tortuosity is constant, independent of time, for each case in this study.

In the validation of Figure 4, the model is essentially one dimensional, i.e. in the thickness direction. As oxygen transport in ambient air is in general well understood and has been properly incorporated in the present model, the validation can be extended to the case of Figure 3, which contains a gas channel for oxygen supply. Specially, the oxygen transport equation in the channel, in absence of convection, is given by:

$$\frac{\partial C_{O2}}{\partial t} = \nabla \cdot (D_{O2} \nabla C_{O2}) \qquad [39]$$

The diffusivity is estimated through[37]:

$$P \cdot D_{ij} = a \left(\frac{T}{\sqrt{T_{ci} T_{cj}}} \right)^b (P_{ci} P_{cj})^{1/3} (T_{ci} T_{cj})^{5/12} \left(\frac{1}{M_i} + \frac{1}{M_j} \right)^{1/2} \qquad [40]$$

where T is temperature in [K], P is pressure in [atm], D_{ij} is the binary diffusion coefficient in [cm^2/s], and M is the molecular weight in [g/mol]. The subscript c denotes the critical value. The formula is based on the kinetic theory of gas for low pressure. Typically, a and b are set to 2.745 $\times$ 10^{-4} and 1.823 for pair of nonpolar gases, which is the case for oxygen in the air (or O_2-N_2 system). Given T_c and P_c of 154.4/126.2 K and 49.7/33.5 atm for O_2/N_2, respectively, D_{O2} (or D_{O2-N2}) is estimated to be around 2.06 $\times$ 10^{-5} m^2/s under 1 atm and 25 °C, which is close to the value (1.88 $\times$ 10^{-5} m^2/s[38]). To show the 2-D simulation results of a battery with gas channels, we switched the boundary setting back to Figure 3. All the parameters were the same as Figure 4. The simulation predicts almost the same results, including output voltage and quantity distributions. Figures 6–14 present the predicted distributions of the volume fraction of precipitate, oxygen content, and reaction rate, indicating negligible gradients in the along-channel dimension.

Figures 6–8 present the volume fraction of discharge products at different discharging stages (see Figure 4). As discharge products are produced through the ORR, their volume fraction quantifies the overall local reaction rate in the time frame of interest. Figure 6 shows that initially there is a small amount of precipitate, almost evenly distributed across the cathode under for 0.05 mA/cm^2. As discharging proceeds, precipitate accumulates in the pore space, and shows a small gradient across the cathode at the stage (b). The gradient

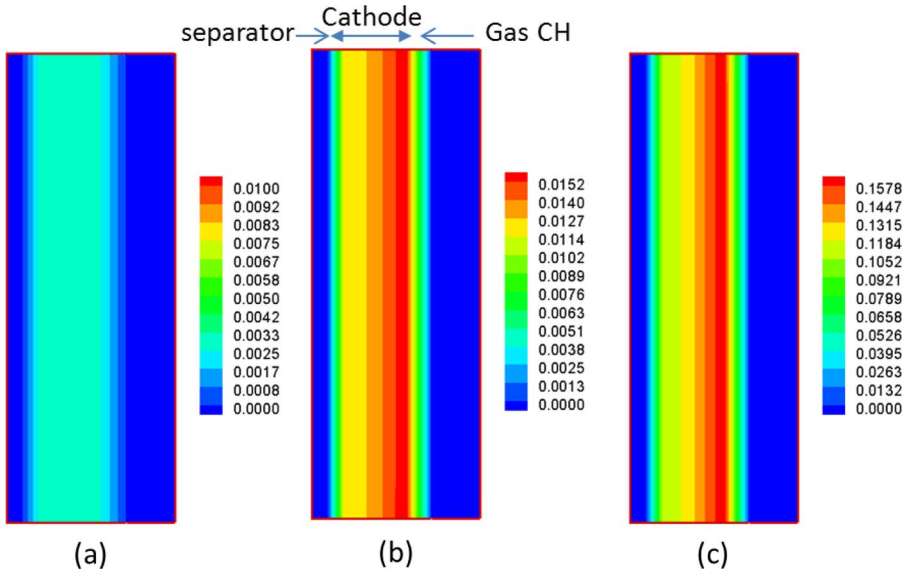

Figure 7. Precipitate volume fraction inside the cathode under the discharging current of 0.1 mA/cm^2 at the stage of (see Figure 4): (a) 7.5 mAh/g; (b) 37.5 mAh/g; (c) 360 mAh/g.

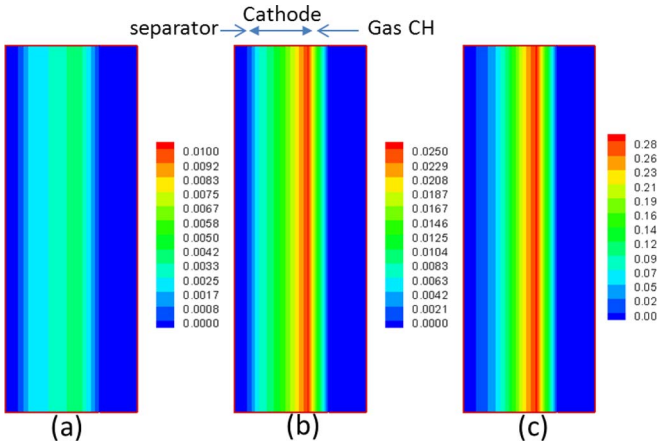

Figure 8. Precipitate volume fraction inside the cathode under the discharging current of 0.2 mA/cm^2 and varying tortuosity at the stage of (see Figure 4): (a) 7.5 mAh/g; (b) 37.5 mAh/g; (c) 360 mAh/g.

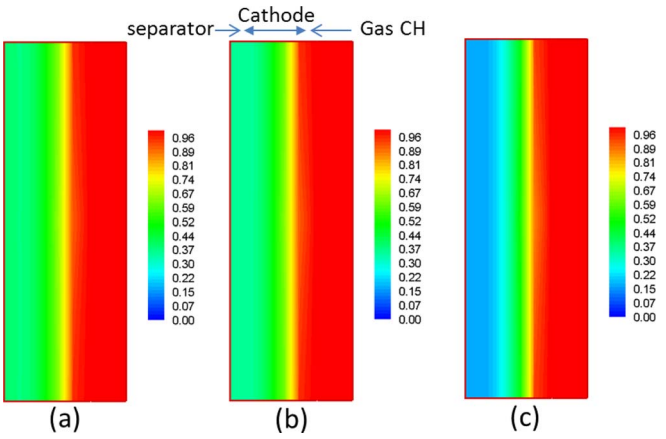

Figure 10. Dimensionless oxygen content in the cathode under 0.1 mA/cm^2 at the stage of (see Figure 4): (a) 7.5 mAh/g; (b) 37.5 mAh/g; (c) 360 mAh/g. The oxygen in the electrolyte is scaled by the value equilibrium to the inlet oxygen concentration; the oxygen content in the channel is scaled by the inlet value.

enlarges as discharging further proceeds as a result of specially varying reaction rate. In the stage (e) which is near shut down, the inner cathode contains about 40% volume fraction of insoluble products, while ∼60% is occupied in the outer cathode. Nanda et al.[17] also observed more discharging product formation near the electrode edge.

Figure 7 displays the distribution under *0.1 mA*/cm^2, showing a similar trend: the gradient enlarges as discharging proceeds. Comparing with *0.05 mA*/cm^2, the gradient is larger under the same discharging stage. For example, the stage (c) has about 16% of precipitate occupied the outer cathode under *0.1 mA*/cm^2, whereas <14% for *0.05 mA*/cm^2. This is due to the spatial variation of the ORR, which is more severe under *0.1 mA*/cm^2, to be presented later.

Figure 8 displays the contours under 0.2 mA/cm^2, showing discernable gradients even at the initial stage (a). At the stage (b), the outer and inner cathode has over 5% and about 1% volume fraction of precipitate, respectively. At the stage (c), over 35% volume space of pores is occupied by precipitates in the outer cathode, while about 5% in the inner one. It is clear that under higher currents the gradient is larger, thus more cathode pore space is unavailable for storing Li oxides. As a result, the specific capacity (either per volume or per weight) suffers.

Figures 9–11 present oxygen content contours in the Li-air battery. Under *0.05 mA*/cm^2, initially (a and b) the oxygen content decreases to about 60% in the inner cathode. At the latter stage, e.g. (d), the oxygen content near the separator decreases to nearly 0. At the stage (e) that is near the battery's shut down, the majority area is subject to zero oxygen content, thus is inactive in the ORR reaction. The observed oxygen starvation occurs as a result of precipitate accumulation in pores: Figure 5 shows that almost 60% of the pore space is occupied by insoluble products in the outer cathode.

In Figure 10, it is seen that the initial stages (a) and (b) under *0.1 mA*/cm^2 exhibit lower oxygen content than under *0.05 mA*/cm^2 due to the larger oxygen consumption rate. In the stage (c), the oxygen content decreases to below 20% under *0.1 mA*/cm^2, showing that local oxygen starvation occurs earlier. Figure 11 shows that the oxygen content is almost zero in the inner cathode even at the initial stage (a and b) under *0.2 mA*/cm^2. Oxygen can only penetrate a very short distance into the cathode surface to sustain the applied electric current. As the discharging proceeds toward the final stage (c), more inner region is inaccessible to oxygen.

Figures 12–14 present the local ORR reaction rate within the cathode. Under 0.05 mA/cm^2, the reaction is nearly uniform in the cathode at the initial stage (a). As discharging proceeds, the spatial variation of ORR becomes evident: in the stage (c and d), a clear gradient develops, as a result of spatially varying oxygen and insoluble precipitate contents (see Figure 6 and 9). The maximum ORR rate occurs at the cathode's surface or the boundary of the gas channel and cathode, where oxygen in the channel easily accesses. In the stage (e), the

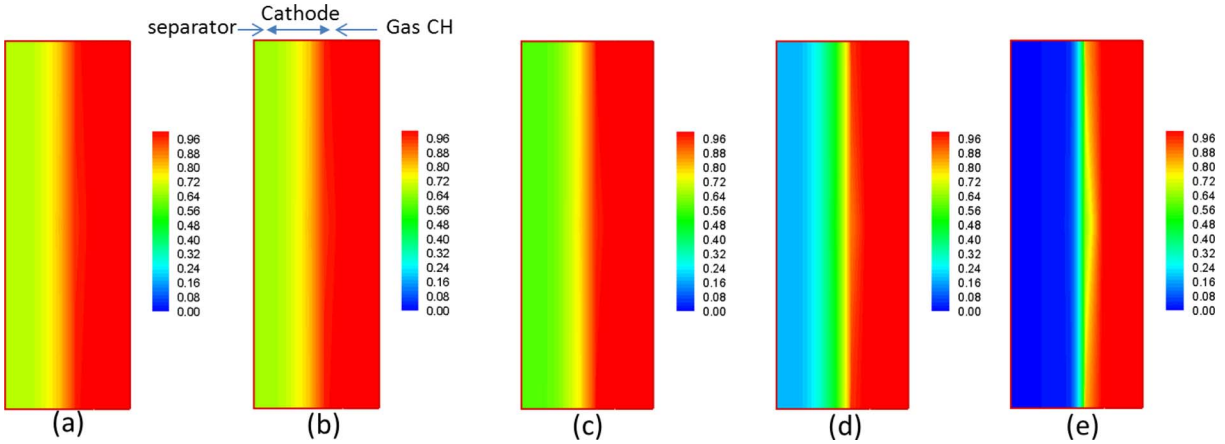

Figure 9. Dimensionless oxygen content in the cathode under 0.05 mA/cm^2 at the stage of (see Figure 4): (a) 7.5 mAh/g; (b) 37.5 mAh/g; (c) 360 mAh/g; (d) 1080 mAh/g; (e) 1360 mAh/g. The oxygen in the electrolyte is scaled by the value equilibrium to the inlet oxygen concentration; the oxygen content in the channel is scaled by the inlet value.

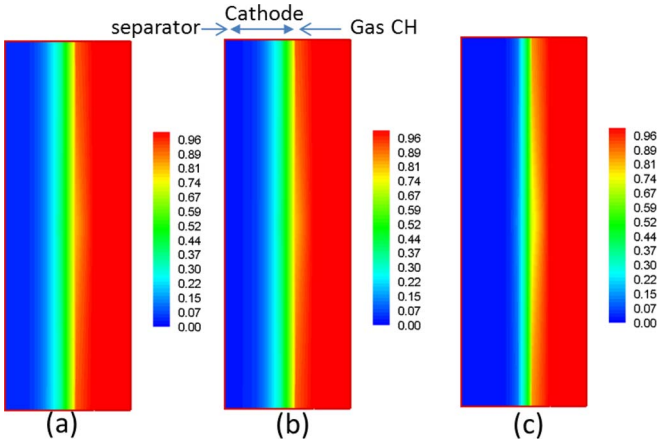

Figure 11. Dimensionless oxygen content in the cathode under 0.2 mA/cm^2 and tortuosity of 1.5 at the stage of (see Figure 4): (a) 7.5 mAh/g; (b) 37.5 mAh/g; (c) 360 mAh/g. The oxygen in the electrolyte is scaled by the value equilibrium to the inlet oxygen concentration; the oxygen content in the channel is scaled by the inlet value.

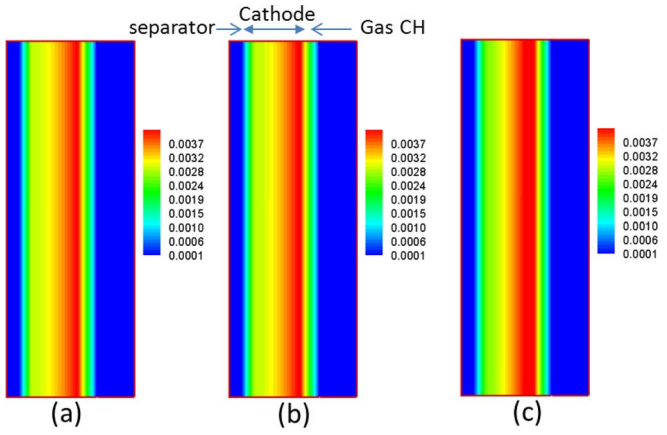

Figure 13. Local ORR reaction rate (oxygen consumption rate[mol/s m^3]) at 0.1 mA/cm^2 at the stage of (see Figure 4): (a) 7.5 mAh/g; (b) 37.5 mAh/g; (c) 360 mAh/g.

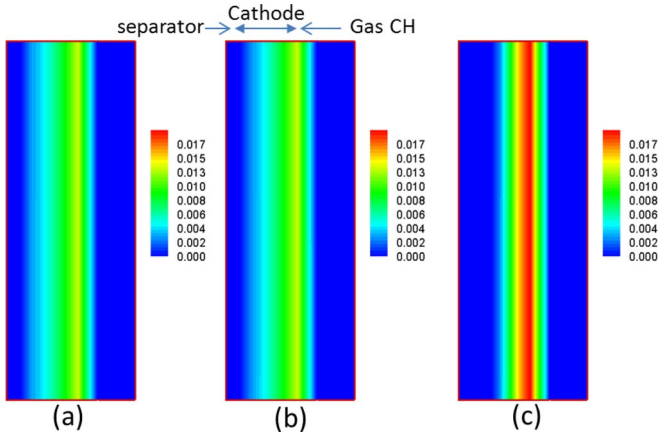

Figure 14. Local reaction rate (oxygen consumption rate [mol/s m^3]) under 0.2 mA/cm^2 and the tortuosity of 1.5 at the stage of (see Figure 4). (a) 7.5 mAh/g; (b) 37.5 mAh/g; (c) 360 mAh/g.

cathode inner portion is inactive in the ORR due to lack of oxygen access. Figure 13 indicates a clear gradient in the reaction rate at the initial stages (a and b) under *0.1 mA/*cm^2, which again arises from the oxygen transport resistance in the cathode (see Figure 10). Note that initially little precipitate is built up (see Figure 7a), yielding a small impact on the reaction surface coverage. For *0.2 mA/*cm^2, Figure 14 shows that the spatial variation is more severe: in the inner cathode, the ORR is inactive even at the initial stages (a and b). As seen from Figure 11a and 11b, little oxygen penetrates into the inner area, yielding the observed almost zero ORR rate. At the stage (c), only the fairly narrow area near the cathode outer surface remains active in the ORR. It is clear that the oxygen resistance is a major limiting factor for local ORR rate. To improve ORR, one can use electrolytes with a large oxygen diffusivity or pressurized oxygen for the cathode reaction.

The channel depth in the preceding cases is 0.8 mm, comparable with the cathode thickness, therefore adding a considerable volume to the battery and hence reducing its specific energy. The prediction indicated almost uniform oxygen in the channel, so the supply is sufficient. Thus, the channel dimension can be further reduced without sacrificing oxygen supply. The benefit of using a small channel depth is the smaller battery volume or increased specific energy (per volume). We also investigated the channel depth reduced by 10 times, i.e. 80 μm, and obtained almost the same contours of oxygen in the channel. Note that this depth (80 μm) yields a channel that adds negligible volume to the battery. Another dimension to increase energy density is along the channel by reducing inlet/outlet manifolds, i.e. a single channel serves more reaction area with oxygen supply. To further explore the limit for oxygen transport resistance, the channel depth is kept at 80 μm with its length extending from 2 cm to

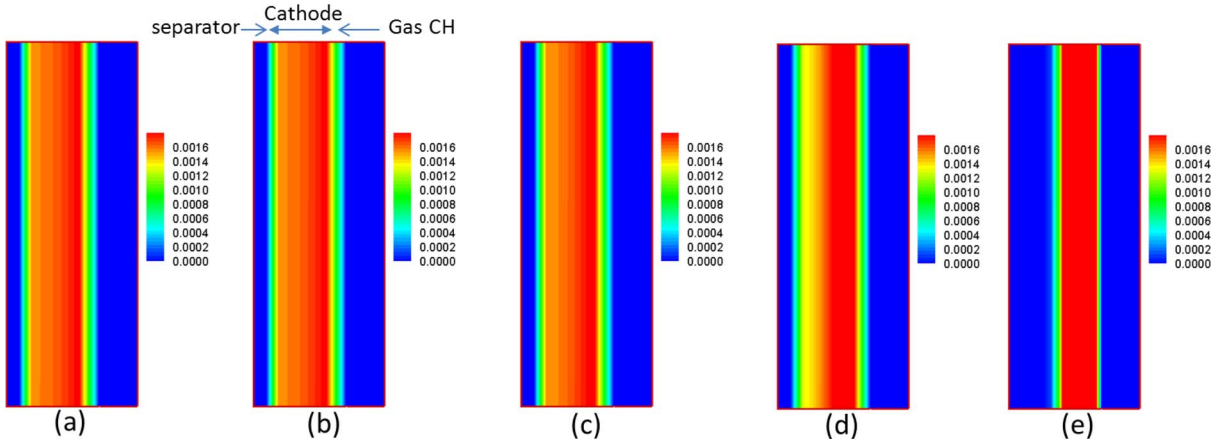

Figure 12. Local ORR reaction rate (oxygen consumption rate [mol/s m^3]) in the cathode under 0.05 mA/cm^2 at the stage of (see Figure 4). (a) 7.5 mAh/g; (b) 37.5 mAh/g; (c) 360 mAh/g; (d) 1080 mAh/g; (e) 1360 mAh/g.

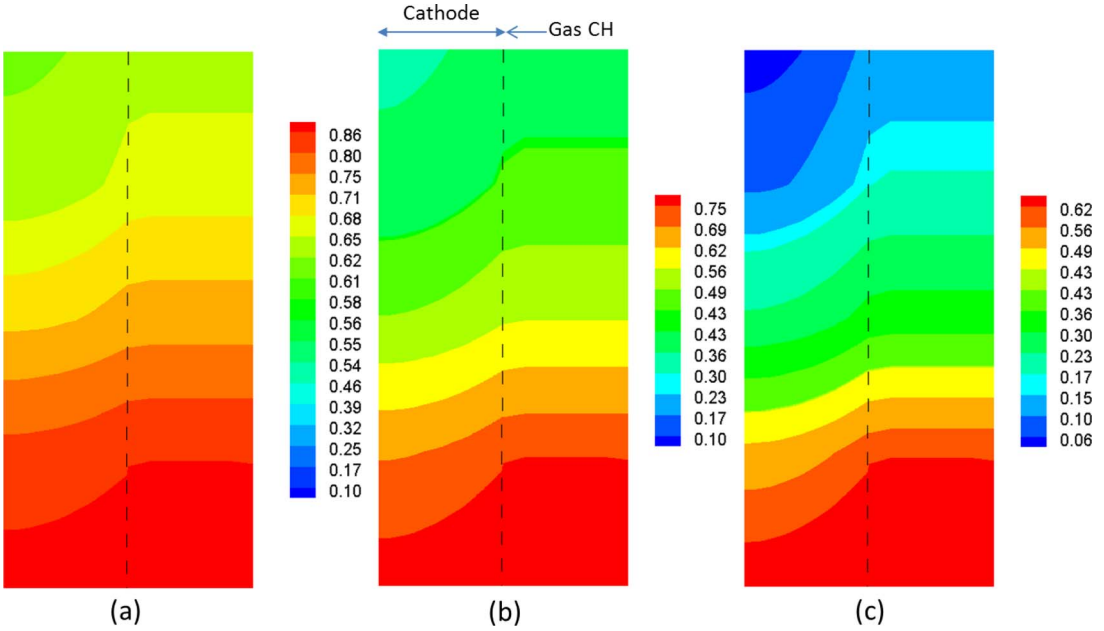

Figure 15. Dimensionless oxygen content in the cathode under (a) 0.05 mA/cm^2; (b) 0.1 mA/cm^2; and (c) 0.15 mA/cm^2 for a Li-air battery with a channel depth of 80 μm and length of 10 cm. The oxygen in the electrolyte is scaled by the value equilibrium to the inlet oxygen concentration; the oxygen content in the channel is scaled by the inlet value.

10 cm. We replaced pure oxygen by ambient air for the cathode. Figure 15 presents oxygen contours, showing considerable variation in the channel even under 0.05 mA/cm^2. For 0.15 mA/cm^2, the inner channel has an oxygen content around 10% of its inlet value, indicating oxygen starvation may occur.

For analysis purpose, a simplified case is considered below, with a focus on the along-channel oxygen transport. Steady state is assumed, justified through the below time constant analysis:

$$\tau_{D,O2} = \frac{L^2}{D_{O2}} \qquad [41]$$

$\tau_{D,O2}$ is ~20 s for L of 2 cm; and ~500 s for L of 10 cm. Both are small comparing with the time span of a single battery discharging operation. Assuming a uniform current density I along the channel, see Figure 16, the oxygen concentration can be obtained by solving the 1-D oxygen conservation equation:

$$\frac{C_{O2} - C_{O2,0}}{C_{O2,0}} = Da\left(\frac{1}{2}\bar{x}^2 - \bar{x}\right) \qquad [42]$$

where $\bar{x} = \frac{x}{L}$ and the Damköhler number $Da = \frac{IL^2}{4F\delta D_{O2}C_{O2,0}} = \frac{\text{reaction rate}}{\text{transport rate}}$

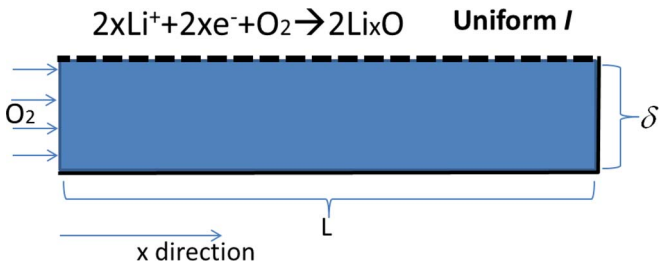

Figure 16. Schematic of oxygen transport in the gas channel of a Li-air battery for analysis.

The maximum variation is then given by:

$$\frac{C_{O2,0} - C_{O2}(\bar{x} = 1)}{C_{O2,0}} = \frac{Da}{2} \qquad [43]$$

It is seen that both the channel depth δ and length L impact oxygen concentration. In this study, Da is ~0.0007 (for Figure 6 with a channel depth of 0.8 mm), ~0.007 (for the battery in Figure 6 with a 80 μm depth), and ~0.8 (for Figure 15 using ambient air) under 0.05 mA/cm^2. These values are consistent with the numerical simulation results. As the Da value becomes larger, the assumption of uniform current density fails, thus Eq. 43 becomes invalid. In practice, the Da value needs to be kept low to avoid local concentration voltage loss.

Conclusions

This work presented a two-dimensional modeling study on Li-air batteries. The model consists of a set of conservation equations for charges, oxygen, and Li^+, in conjunction with the electrochemical reaction kinetics and mechanisms of discharge precipitate's impact on voltage loss. The model was validated with experimental data for 0.05 and 0.1 mA/cm^2, using the same set of parameters. For 0.2 mA/cm^2, a different tortuosity in the cathode showed a better match with the experimental data. SEM images indicated that the precipitate's morphology differs under different currents, likely yielding different tortuosity. Through simulation results, we found that at initial discharging oxygen is able to penetrate into the cathode for 0.05 and 0.1 mA/cm^2; whereas under 0.2 mA/cm^2 oxygen is inaccessible to the inner cathode, yielding local inactive ORR. As discharging proceeds, insoluble precipitate accumulated, reducing oxygen penetration into the cathode. Near the shutdown of discharging (or the cut-off voltage), the ORR was inactive in the majority portion of the cathode under 0.2 mA/cm^2. The cathode pore space is not fully utilized to store discharging products, specially under high current density. In addition, the oxygen profile in the channel was analyzed and related to the Damköhler (Da) number. The analytical results of the oxygen concentration variation along the channel were consistent with the simulation results. The developed virtual tool can be used to optimize cathode structure, examine new materials and configuration, and battery geometry for high performance, cost effective Li-air batteries.

Acknowledgment

We gratefully acknowledge the support of the National Science Foundation (CBET-1336873) on this study.

List of Symbols

a	factor of effective catalyst area per unit volume when discharge product is present; a coefficient in diffusivity calculation
a_o	factor of initial catalyst surface area per unit volume
C	molar concentration of species k, mol/m^3
D	species diffusivity, m^2/s
Da	the Damköhler number
F	Faraday's constant, 96,487 C/mol
I	current density, A/cm^2
i	superficial current density, A/cm^2
j	transfer current density, A/cm^3
M	molecular weight, kg/mol
R	universal gas constant, 8.134 J/mol K; Ohmic resistance, mΩ cm^2
s	volume fraction of precipitate in void space
t	time, s
T	temperature, K
E_o	equilibrium potential, V

Greek

β	transfer coefficient
ρ	density, kg/m^3
ϕ	phase potential, V
κ	ionic conductivity, S/m
ε	porosity or volume fraction
η	surface overpotential, V
τ	tortuosity; coverage coefficient; time constant, s
δ	thickness, m
σ	electronic conductivity, S/m;

Superscripts and Subscripts

c	cathode
d	diffusion
e	electrolyte
eff	effective value
film	precipitate film
o	reference value; initial value
prod	discharge product
s	solid phase

References

1. S. J. Visco, E. Nimon, B. Katz, L. C. D. Jonghe, and M. Y. Chu, *The 12th International Meeting on Lithium Batteries Abstract*, Nara, Japan, Abstr., No. 53, 2004.
2. J. Fu, U.S. Patent 5702995, 1997.
3. T. Zhang, N. Imanishi, Y. Takeda, and O. Yamamoto, *Chem. Lett.*, **40**, 668 (2011).
4. T. Ogasawara, A. Debart, M. Holzapfel, P. Novak, and P. G. Bruce, *J. Am. Chem. Soc.*, **128**, 1390 (2006).
5. S. A. Freunberger, Y. Chen, Z. Peng, J. M. Griffin, L. J. Hardwick, F. Bardé, P. Novák, and P. G. Bruce, *J. Am. Chem. Soc.*, **133**, 8040 (2011).
6. W. Xu, J. Xiao, J. Zhang, D. Wang, and J. G. Zhang, *J. Electrochem. Soc.*, **156**, A773 (2009).
7. O. Crowther, D. Keeny, D. M. Moureau, B. Meyer, M. Salomon, and M. Handricson, *J. Power Sources*, **202**, 347 (2012).
8. S. S. Zhang, K. Xu, and J. Read, *J. Power Sources*, **196**(8), 3906 (2011).
9. P. Albertus, G. Girishkumar, B. McCloskey, R. S. Sánchez-Carrera, B. Kozinsky, J. Christensen, and A. C. Luntz, "Identifying Capacity Limitations in the Li/Oxygen Battery Using Experiments and Modeling," *Journal of The Electrochemical Society*, **158**, A343 (2011).
10. M. Mirzaeian and P. J. Hall, *Electrochim. Acta.*, **54**, 7444 (2009).
11. C. Tran, X. Q. Yang, and D. Qu, *J. Power Sources*, **195**(7), 2057 (2010).
12. J. Xiao, D. Mei, X. Li, W. Xu, D. Wang, G. L. Graff, W. D. Bennett, Z. Nie, L. V. Saraf, I. A. Aksay, J. Liu, and J. G. Zhang, *Nano Lett.* **11**, 5071 (2011).
13. H. Cheng and K. Scott, *J. Power Sources*, **235**, 226 (2013).
14. V. Viswanathan, K. S. Thygesen, J. S. Hummelshøj, J. K. Nørskov, G. Girishkumar, B. D. McCloskey, and A. C. Luntz, "Electrical conductivity in Li_2O_2 and its role in determining capacity limitations in non-aqueous Li-O2 batteries," *J. Chem. Phys.*, **135**, 214704 (2011).
15. R. R. Gagne, Carl A. Koval, and George C. Lisensky, "Ferrocene as an internal standard for electrochemical measurements," *Inorg. Chem.*, **19**(9), 2854 (1980).
16. Y. C. Lu, D. G. Kwabi, K. P. C. Yao, J. R. Harding, J. Zhou, L. Zuin, and Y. Shao-Horn, *Energy Environ. Sci.*, **4**, 2999 (2011).
17. J. Nanda, H. Biheux, S. Voisin, G. M. Veith, R. Archibald, L. Walker, S. Allu, N. D. Dudney, and S. Pannala, *J. Phys. Chem. C*, **116**, 8401 (2012).
18. B. M. Gallant, R. R. Mitchell, D. G. Kwabi, J. Zhou, L. Zuin, C. V. Thompson, and Y. Shao-Horn, *J. Phys. Chem. C*, **116**, 20800 (2012).
19. P. Andrei, J. P. Zheng, M. Hendrickson, and E. J. Plichta, *J. Electrochem. Soc.*, **159**(6), A770 (2012).
20. X. Ren, S. S. Zhang, D. T. Tran, and J. Read, *J. Mater. Chem.*, **21**, 10118 (2011).
21. U. Sahapatsombut, H. Cheng, and K. Scott, *Journal of Power Sources*, **227**, 243 (2013).
22. Y. Wang, *Electrochimica Acta*, **75**, 239 (2012).
23. Y. Wang and S. C. Cho, "Analysis of Air Cathode Performance for Lithium-Air Batteries." *Journal of The Electrochemical Society*, **160**(10), A1847 (2013).
24. M. W. Chase Jr., *Journal of Physical and Chemical Reference Data Monographs*, **9**, 1510 (1998).
25. Y. C. Lu, H. A. Gasteiger, M. C. Parent, V. Chiloyan, and Y. Shao-Horn, *Electrochemical and Solid-State Letters*, **13**, A69 (2010).
26. U. Sahapatsombut, H. Cheng, and K. Scott, *J. Power Sources*, **243**, 409 (2013).
27. C. O'Laoire, S. Mukerjee, K. M. Abraham, E. J. Plichta, and M. A. Hendrickson, *J. Phys. Chem. C, J. Phys. Chem. C*, **114**, 9178 (2010).
28. G. K. Batchelor, Brownian diffusion of particles with hydrodynamic interaction, *Journal of Fluid Mechanics*, **74**, 1 (1976).
29. W. M. Deen, *Analysis of Transport Phenomena*, Oxford University Press (1998).
30. M. J. Martínez, S. Shimpalee, and J. W. Van Zee, "Measurement of MacMullin Numbers for PEMFC Gas-Diffusion Media," *Journal of The Electrochemical Society*, **156**(1), B80 (2009).
31. Y. Wang, K. S. Chen, and S. C. Cho, *PEM Fuel Cells: Thermal and Water Management Fundamentals (Sustainable Energy)*, Momentum Press (2013).
32. S. G. Stewart and J. Newman, *Journal of The Electrochemical Society*, **155**, F13 (2008).
33. A. Nyman, M. Behm, and G. Lindbergh, *Electrochimica Acta*, **53**, 6356 (2008).
34. M. Doyle, J. Newman, A. S. Gozdz, C. N. Schmutz, and J.-M. Tarascon, *J. Electrochem. Soc.*, **143**, 1890 (1996).
35. S. V. Patankar, *Numerical Heat Transfer and Fluid Flow*, Hemisphere Publishing Corp., New York (1980).
36. J. Read, *J. Electrochem Soc.*, **149**, A1190 (2002).
37. R. Byron Bird, Warren E. Stewart, and Edwin N. Lightfoot, *Transport phenomena*, John Wiley & Sons (2007).
38. Y. Wang, "Analysis of the Key Parameters in the Cold Start of Polymer Electrolyte Fuel Cells," *J. Electrochem. Soc.*, **154**, B1041 (2007).
39. J. Read and Y. Wang, Private Communication.
40. J. Read, K. Mutolo, M. Ervin, W. Behl, J. Wolfenstine, A. Driedger, and D. Foster, *J. Electrochems Soc.*, **150**, A1351 (2003).
41. X. Z. Wu, T. Morikawa, K. Uchiyama, and T. Hobo, *J. Phys. Chem. B*, **101**, 1520 (1997).
42. C. O. Laoire, S. Mukerjee, K. M. Abraham, E. J. Plichta, and A. Hendrickson, *J. Phys. Chem. C*, **113**, 20127 (2009).
43. H. Dai, S. Sanderson, J. Davey, F. Uribe, and T. A. Zawodzinski, *Electrochem. Soc. Proceedings Volume*, **96–17**, 111 (1997).
44. A. D. Pasquier, C. Sarrazin, X. Andrieu, and J. F. Fauvarque, *Electrochem. Soc. Proceedings Volume*, **96–17**, 14 (1997).
45. S.-Y. Kishioka, *Electroanalysis*, **13**, 1161 (2001).
46. M. Tsushima, K. Tokuda, and T. Ohsaka, *Anal. Chem.*, **66**, 4551 (1994).
47. H. S. Choe, B. G. Carroll, D. M. Pasquariello, and K. M. Abraham, *Chem. Mater.*, **9**, 369 (1997).